www.sciencemag.org/cgi/content/full/340/6137/1196/DC1

Supplementary Materials for

Probing the Solar Magnetic Field with a Sun-Grazing Comet

Cooper Downs,* Jon A. Linker, Zoran Mikić, Pete Riley, Carolus J. Schrijver, Pascal Saint-Hilaire

*Corresponding author. E-mail: cdowns@predsci.com

Published 7 June 2013, *Science* **340**, 1196 (2013)
DOI: 10.1126/science.1236550

This PDF file includes:

Other supplementary material for this manuscript includes the following:

Movies S1 to S8

Materials and Methods

Observations and Data Analysis: The perihelion passage of Comet C/2011 W3 (Lovejoy) was observed in the low corona from three vantage points. At Earth, perihelion was imaged by the Atmospheric Imaging Assembly (AIA) (*17*) onboard SDO, which obtains high resolution (4096×4096) EUV images every 12 seconds in seven EUV wavelengths. The closest approach was obscured by the solar disk, but the high cadence, multi-wavelength imaging allowed the ingress and egress from behind the disk to be imaged in detail from approximately 1-1.9 and 1-1.4 R_S respectively. Analysis of the multi-wavelength comet tail emission observed by AIA is given by (*7*), and further analysis involving X-Ray imaging data is given by (*18*). Both studies find emission profiles consistent with water ice as a source for emitting oxygen ions, which we consider in this work. During perihelion the STEREO A and B spacecraft (*19*) were separated from Earth by 109 and $107°$, offering two complementary vantage points. EUV emission from the comet was imaged at a 75-150s cadence in the 171Å channel by the EUVI A and B instruments (*20*). The EUVI 171 and AIA 171Å channels have similar spectral widths and are designed to isolate the strong FeIX coronal emission line, which is characteristic of 0.7-1.2 MK coronal plasma. In the case of cometary tail plasma, the high abundance of oxygen also implies a strong contribution to the 171Å channel due to the nearby OV and OVI lines, which can easily dominate cometary Fe emission (*7*).

Base ratio images are generated by dividing the flux of each pixel at the current time by the flux of the nearest pre-flyby state. This serves to highlight the local enhancement of EUV intensity over the background due to the presence of emitting cometary tail ions. To enhance the signal-to-noise ratio for weak intensity signals off of the solar disk, every other AIA image was stacked together (i.e. temporally binned to 24s cadence) after being spatially binned by a factor of two. All base ratio observations shown here are linearly scaled from $1 \pm 0.3, 0.4, 0.3, 0.2$ for

EUVI-A, EUVI-B, AIA ingress, and AIA egress respectively (chosen for optimal contrast).

Additionally, the trajectory used in this work is obtained from (*3*). Further timings refinements made comparing this trajectory to spacecraft data can be found in (*21*). Movies S1-S4 show animations the base ratio processed 171Å observations for each view with the comet trajectory overlaid. The intersection of the moving horizontal and vertical lines indicates the predicted position of the comet nucleus at the observation time, which is offset according to the light travel time from the sun to to each spacecraft.

Numerical Model: To simulate the inhomogeneous plasma conditions of the global corona at time of the comet passage we use the 3D Magnetohydrodynamic Algorithm outside a Sphere (MAS) code. MAS solves the resistive thermodynamic MHD equations on a nonuniform (r, θ, ϕ) mesh using a massively parallel semi-implicit time-stepping algorithm. The method of solution, including the boundary conditions, has been described previously (*22–27*). For this simulation, we run MAS on over a thousand processors using a relatively high resolution 181x191x401 mesh with angular resolution concentrated in regions where the comet passed.

A primary application of MAS is to simulate realistic magnetic configurations that are observed in the corona, which is achieved by using observational measurements of the photospheric magnetic field as boundary conditions. For this case we use a 'synchronic' magnetic field map of SDO/HMI observations (*28*) developed to represent the conditions at 23:45:01 UT on 2011/12/25 using the method described by (*29*). This map is shown in Fig. S1. A synchronic map is designed to represent the entire photospheric flux-distribution at a given instance in time and is built by continuously evolving photospheric flux in time according to a known prescription for surface flows and the emergence and cancellation of small scale flux distributions (the so called salt and pepper). A continuous assimilation of full disk line-of-sight field data from the front-side of the sun into the model keeps the map as up to date as possible with the current

observable photospheric conditions. For this study, the magnetogram assimilation code was revised to use SOHO/MDI observations (*30*) at calibration level 1.8 instead of quicklook data, to correct for a nonuniform zero-point offset of the SOHO/MDI magnetograms, to correct a minor error coordinate transformations from observed magnetograms to heliocentric coordinates, to use the updated SDO/HMI calibration from (*31*), and to initialize from a field configuration 1.3 times stronger in 1996.5 for a better comparison with SOHO/MDI synoptic maps throughout the overlapping assimilation period (1996.5-2010.5).

A full visualization of the 3D magnetic field solution along the trajectory is shown in Fig. S2. Because the comet perihelion takes it so deep into the corona (closest approach is approximately 1.2 R_S), much of the trajectory intersects closed field streamer regions, which are highlighted in blue.

The 'thermodynamic' element of the model refers to the incorporation of a realistic MHD energy equation into the algorithm. The additional non-ideal thermodynamic terms include anisotropic thermal conduction along the magnetic field, optically thin radiative losses by coronal plasma, and an empirically developed volumetric coronal heating function (*25–27, 32*). Although computationally intensive, capturing these essential terms provides a realistic thermal equilibrium for the 3D distribution of plasma temperature and density. From this we can generate synthetic observables, such as multi-wavelength EUV emission for direct comparison for observational data, a technique used in a variety of recent studies (*32–35*). These comparisons serve as a powerful constraint of model parameters due to the strong dependencies on the local plasma state for a given emission line. In Fig. S3 we show a comparison of AIA 171, 193, 211, and 335Å images generated from the MHD model to observations on 11/27/2012, which capture the perihelion region of the corona as it was last observed by AIA before it rotated out of view. This comparison was used to benchmark and constrain the overall thermodynamic properties of the solution (electron density, temperature, and relative contrasts between regions)

to be observationally consistent for this time period. To determine emissivities we use the CHIANTI 7.1 spectral synthesis package (*36*) and the latest post-launch calibration data available from the SDO/AIA team, which includes cross-calibration with SDO/EVE (*37*). Intrinsic uncertainties include the choice of tabulated ionization equilibrium and abundance tables from the CHIANTI database. Please note that for the zoomed in 171Å comparison shown in Fig. 2 (main text), the details of the coronal loops most visible in the left panel, which result from fine-scale, time-dependent coupling of the plasma dynamics and heating are not expected to be captured at this resolution.

A last implicit assumption of the MHD model when using fixed boundary conditions is that the low corona is in a near steady state at the time of interest. This is not always the case during dynamic events such as coronal mass ejections (CMEs), which can cause perturbations to large-scale field and plasma structures. We conducted a visual inspection of the pre-perihelion corona using coronagraph data from LASCO/C2 (*38*), which observes the corona from around $2{-}6\ \mathrm{R}_S$, and confirmed that the global structure of the corona was relatively static and unperturbed at this time. Furthermore, there were no significant CME's reported in the LASCO CME catalog (*39*) within ~ 23 hours, and the minor events did not have trajectories intersecting the projected path of the comet in the EUV within ~ 16 hours. Given that the low corona will relax on shorter timescales (on the order of tens of minutes to hours), this justifies the use of static boundary conditions for interpreting field orientations in the low corona near perihelion.

On the Assumption of Parallel Flows: To greatly simplify the physical problem of comet tail motion in the corona, we assume a locally fixed magnetic field and consider tail ions flowing parallel to it. This approximation neglects the potential modification of the ambient field by electric currents produced when the total momentum exchange between tail ions and the coronal plasma becomes non-negligible. As discussed by (*4*), the regime where this becomes important,

as it was for the Comet 2011/N3 (SOHO), is highly sensitive to the size of the nucleus, sublimation rate, and local field magnitude. In Lovejoy's case, except for a conspicuous region of the ingress observed by AIA around 23:58-00:01 UT, where a non-negligible component of motion appeared to be backwards along the orbit (see movie S1), the strong preference for motion out of the orbital path indeed suggests and is consistent with the assumption that field modification did not play a significant role in determining the tail trajectory (this would be a small effect in determining orientation). It is for these practical and physical considerations that we decouple the coronal field from the cometary tail ions, and treat them as test particles in an embedded macroscopic plasma.

S1 Deceleration Timescales

The key timescale that mediates deceleration and diffusion of injected cometary ions is the time in which a series of successive small angle collisions will effectively randomize the initial velocity. Following the introductory discussion in (*40*), this can be parameterized in terms of a collision rate coefficient and effective cross section

$$\nu = \sigma^* n_F v_0, \text{ and } \sigma^* = \frac{1}{2\pi}\left(\frac{q_T q_F}{\epsilon_0 \mu v_0^2}\right)^2 \ln\Lambda \tag{S1}$$

where, the T and F subscripts denote a test and field particle respectively. Assuming thermal equilibrium and therefore an average thermal velocity, an average momentum exchange rate for electron electron collisions can be computed numerically:

$$\nu_{ee} = 10 \times \frac{n_8}{T_6^{3/2}}\left(\frac{\ln\Lambda}{20}\right) \text{ s}^{-1}. \tag{S2}$$

where n_8 is the electron density in units of 10^8 cm^{-3} and T_6 is the electron temperature in units of 10^6 K. Simple arguments give the remaining rates in terms of relative mass fractions, $\nu_{ie} = Z_i^2 \nu_{ee}(m_e/m_i)$, and $\nu_{ip} = Z_i^2 \nu_{pp}(m_p/m_i) = Z_i^2 \nu_{ee}(m_e/m_p)^{1/2}(m_p/m_i)$, where the subscripts i and p refer to the ion species and protons respectively while Z_i is the charge number.

Considering an O^{5+} ion as the test particle and $n_e \sim 10^8$ cm^{-3}, $T_e \sim 1.5$ MK, this gives momentum exchange timescales ($\tau = 1/\nu$) of $\tau_{ie} \sim 220$ s and $\tau_{ip} \sim 5.0$ s respectively, where the shorter ion-proton timescale as well as the $n/T^{3/2}$ and Z_i^2 dependencies should be noted.

At first glance τ_{ip} appears to be too short for cometary ions to travel an appreciable distance before thermalizing with the medium; a particle with velocity of 500 km s^{-1} only moves 0.0025 R_S in this time, while the tail moves more than 0.1 R_S perpendicular to the orbit in some places. While the simplest rate calculation outlined above is correct for in-equilibrium conditions, the resolution of this discrepancy comes by recognizing the importance of the initial relative velocity of cometary ions with respect to the medium. Considering outflowing cometary ions as an a mono-energetic beam of test particles with a mean velocity u and the field plasma as being Maxwellian, (*40*) outlines a formal solution of the Fokker-Planck equation to find the 'slowing down' equation for effective deceleration $\partial u/\partial t$ of the velocity as a function of time. This takes the form

$$\frac{\partial u}{\partial t} = \frac{n_e e^4 Z_i^2 \ln\Lambda}{4\pi\epsilon_0^2 m_i^2}\left[\left(1+\frac{m_i}{m_p}\right)\frac{m_p}{2k_B T_p}\frac{\mathrm{d}}{\mathrm{d}\xi_p}\left(\frac{\mathrm{erf}(\xi_\mathrm{p})}{\xi_p}\right)+\left(1+\frac{m_i}{m_e}\right)\frac{m_e}{2k_B T_e}\frac{\mathrm{d}}{\mathrm{d}\xi_e}\left(\frac{\mathrm{erf}(\xi_\mathrm{e})}{\xi_e}\right)\right] \tag{S3}$$

where $\xi_{i,e} = u\sqrt{m_{p,e}/2k_B T_{p,e}}$. The two bracketed terms represent the effective friction of the protons and ions respectively, and their relative importance depends on the ion beam speed relative to the thermal speed of the field species. An effective timescale for deceleration can then be written as $\tau_d = -u/(\partial u/\partial t)$. This timescale can be evaluated numerically, but we find it instructive to consider the following limiting cases: First, if we approximate τ_d to depend weakly on u, then

$$u = u_0 \exp(-t/\tau_d), \tag{S4}$$

where u_0 is the initial speed. In the limit where the ion velocity is lower than the mean thermal speed of protons, ($u < \langle v_p \rangle$), τ_d is independent of u and becomes comparable to τ_{ip}. Finally, in the case that the ion speed is larger than mean the thermal speed of protons (i.e. when the ion is

injected with speed $u \sim 500 \cos\theta \gtrsim \langle v_p \rangle \sim$ 1-2 $\times 10^2$ km s^{-1}), τ_d calculated from Eq. (S3) takes the form

$$\tau_d \sim \frac{4\pi\epsilon_0^2 m_i^2}{n_e e^4 Z_i^2 \ln\Lambda \left[\left(1+\frac{m_i}{m_p}\right)\frac{1}{u^3} + \left(1+\frac{m_i}{m_e}\right)\left(\frac{m_e}{2k_B T_e}\right)^{3/2}\frac{4}{3\sqrt{\pi}}\right]}. \tag{S5}$$

Here the relative importance of proton collisions is mediated by the $1/u^3$ term while the term due to electron collisions reflects only the ambient temperature of the plasma. This implies that for ion velocities *above* the mean proton thermal speed of the medium, τ_d may be substantially larger than τ_{ip} but smaller than the electron timescale τ_{ie}.

This discussion underscores the following important point: under these assumptions, the deceleration of cometary ions injected into the corona will initially reflect the velocity of the comet projected along the magnetic field. Only after a sufficient timescale for deceleration (one that is magnified by higher parallel velocities and lower coronal densities) will the tail slow to reflect the ambient flow of the embedded medium. That the deceleration timescale may easily be of the order 10^2s in the low corona, and larger than one might naively predict from a thermal equilibrium argument, naturally allows for the EUV comet tail to deviate an appreciable distance from the original orbital plane as its ions flow along the embedded magnetic field. As a first approximation, we use Eq. (S4) for the deceleration of the cometary ions in this work, but with a slightly longer τ_d than would be computed from Eq. (S5).

Diffusion: Once the deceleration process is complete we are left with a mixture of cometary ions and coronal plasma in thermal equilibrium. Given that the fractional abundance of oxygen is 0.3 for the comet (*41*) and $\sim 10^{-3}$ for the corona (*42*), it is reasonable to expect that the mixture will posses an enhanced abundance of oxygen relative to that of the ambient corona (which is, in fact, partially why it is observed over the background in the EUV in the first place). Tracking the relative position of the material after thermalization reduces to a basic

diffusion argument.

Assuming thermal equilibrium, we can compute an effective diffusion coefficient from $D = \nu\lambda_{mfp}^2$, where $\lambda_{mfp} = 1/(\sigma^* n)$ is the mean free path. For a given ion species this reduces to $D_i = k_B T_i / m_i \nu_i$ where $\nu_i = \nu_{ii} + \nu_{ip} + \nu_{ie} \sim \nu_{ip}$ assuming $n_i << n_p$. The diffusion coefficient then allows for the calculation of an effective diffusion length,

$$L_{Di} = 2\sqrt{D_i t} \sim 2\sqrt{\frac{K_B T_i t}{m_i \nu_{ip}}} = 75 \times T_6^{5/4} n_8^{-1/2} \left(\frac{5}{Z_i}\right) \left(\frac{20}{\ln \Lambda}\right) t^{1/2} \text{ km}, \tag{S6}$$

for O^{5+}. In comparison to the scales of the width of the comet tail in the AIA observations ($\sim 1 - 7 \times 10^4$ km), this length on a ten minute time scale is small except in regions where the ambient density is very low. The small relative value of L_{Di} then corroborates the observations of the long lasting portions described in the main text (Figs. 1 and 4), for which the expansion of striations appears to halt after a handful of minutes. That they eventually fade from view on the order of tens of minutes is then likely related to timescale for the specific EUV emitting ionization stages for the bandpass to be surpassed, which will also be inversely proportional to the local electron density (see main text also).

S2 Visualization of the Dynamical Tail Model

As described in the main text, we use the above timescale arguments to simulate and visualize the parallel motion and deceleration of cometary material as it is injected into the inhomogeneous coronal medium. We describe the method and describe the implications for all four views of the comet here. First the comet trajectory is divided up into N spatial locations that correspond to 1 minute intervals along the orbit indexed by n: $\vec{x}_{c,n}(t_n) = \vec{x}_c(t = t_n)$. For each position $\vec{x}_n$ we place two test particles to represent comet ions with speeds representing the orbital velocity projected along $\vec{B}$ and the limiting cases of isotropic outflow velocity of tail ions from the comet body: $\vec{v}_{n\pm} = (\vec{v}_c \cdot \hat{b} \pm v_{out})\hat{b}$.

Starting at time $t = t_n$ (i.e. when the comet passes), the position of the test particles at $\vec{x}_n$ is integrated along $\vec{B}$ using the 3D vector magnetic field field distribution from the MHD model solution. The deceleration of the velocity along $\vec{B}$ is given by Eq. (S4). To capture the effects of ambient flow and diffusion, the local coronal flow vector is added to the velocity, and the diffusion length $L_{Di}(t - t_n)$ from Eq. (S6)) is computed using the mean state of the medium traversed and added to the overall length traveled (*43*). Overall this takes the form

$$\vec{v}_i(t^*, s) = \left[(\vec{v}_c \cdot \hat{b}_0 \ \pm \ v_{out}) \exp(-t^*/\tau_d) + \ \vec{v}_{flow}\right] \hat{b} \tag{S7}$$

for velocity where $t^* = t - t_n$ for $t \geq t_n$. The position follows as:

$$s_i(t^*) = \int_0^{t^*} \vec{v}_i(t, s) \cdot \hat{b}(s) \, \mathrm{d}t \ + \ L_{Di}(t^*), \tag{S8}$$

where $s_i(t^*)$ is the distance traveled along $\vec{B}$ starting from the position $\vec{x}_n$.

The time evolution of this process is overlaid over the observations for all views in Fig. S4 (animated in Movies S5-S8). Initially, two colored test particles are located at rest for each point along the trajectory. The time-dependent position and final resting place of each dot depends on the comet velocity and orientation with respect to $\vec{B}$ according to Eq. (S8). The arrows mark locations where the comet tail is most visible, and highlight comparisons to the model prediction (dots). Animations showing the time-evolution for all for views are also given.

Starting from the AIA ingress view (top row), as the comet encounters the first set of test particles visible (top row, left), Eq. (S8) implies motion in the southwest direction, which is similar to what is observed. Further ahead (top row, middle) the southward extent of the comet declines slightly, and the predicted comet tail positions are deforming similarly. After the comet has passed behind the solar disk (top row, right) the apparent motion of the test particles has roughly ceased because the deceleration/thermalization is effectively complete, which is consistent with the relatively stationary behavior of the long lasting features described in the main text.

The remaining views all have times chosen to illustrate the basic qualitative correlation of the observed comet tail motion with that predicted by the tail model. Each viewpoint shows non-radial and non-orbital test particle motion that varies in space and time. In the EUVI views (middle two rows) the back and forth motion, which might be unexpected for ion tails far from the sun, results quite naturally when considering the low lying closed field topology encountered during closest approach (as seen in Fig. 2). High degrees of field curvature are present and therefore rapidly changing orientations with respect to the comet, $\vec{v}_c \cdot \hat{b}$, are to be expected here. Lastly, the comparison to the egress observations (bottom) does well to highlight the reversal from motion below to above the orbit line, which is similarly implied by the field topology, but now on a larger, smoothly varying scale.

For reference, the locations marked 'A' indicate the extent of this lasting ingress region as it evolves. The observed non-radial and non-tangential direction of motion is captured by the tail model, and this motion is entirely borne out of the projection of the comet orbit with the 3D MHD magnetic field. The discrepancy in total distance is likely related to the inverse density dependence of the deceleration timescale (Eq. (S3)), which is not taken into account by the simple exponential toy model used here to illustrate the qualitative behavior. Similarly, the location marked 'B' highlights the tail as seen by three views at nearly the same state accounting for light travel time. During this part of the post perihelion journey, the comet tail motion has once again become northward of the projected orbit line. This is well matched by the tail model, which predicts this motion based on the alignment of the smoothly varying open field region into which the comet trajectory now passes.

We should also point out here that the exact nature of the non-orbital component of parallel velocity, v_{out}, depends on both the radiation field that photodissociates tail material and on additional interactions with the ambient medium. For example, (*18*) suggest that a pickup-ion-like interaction with the ambient turbulent coronal wave spectrum might relax perpendicular gyro-

motions into a bispherical distribution (*44*) with components along the field proportional to the local Alfvén speed. While this or other relaxation mechanisms potentially represent additional diagnostics, capturing the details of this interaction is significantly more complicated than the collisional deceleration discussed in S1 for parallel flow only. Because these outflow speeds are already secondary velocity components to the orbital motion itself, for our purposes we choose a speed of $v_{out} = 100$ km s^{-1} and use it to illustrate the extremes of observationally plausible values (*7*). Although this speed is too large for exothermic photodissociation reactions involving oxygen alone, we leave the exploration and specification of additional kinetic mechanisms to a future study.

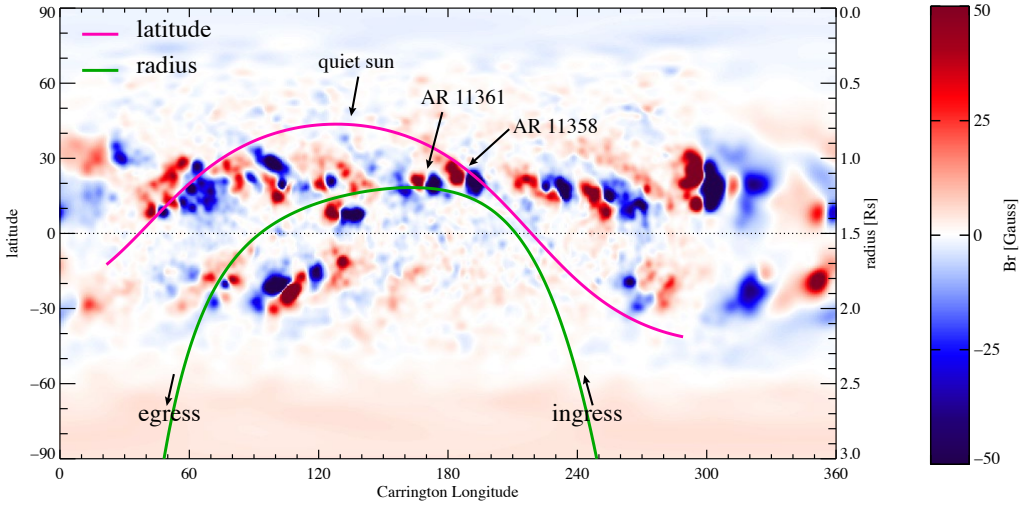

Figure S1: The synchronic map of the radial magnetic field used at the model boundary. The spherical components of the comet trajectory are overlaid to give a sense of the 3D location of the comet with respect to the magnetic field sources. Note that the closest approach is initially near NOAA Active Regions 11361 and 11358 (seen by STEREO-A/B) and the later portion of the trajectory is mostly over the quiet sun.

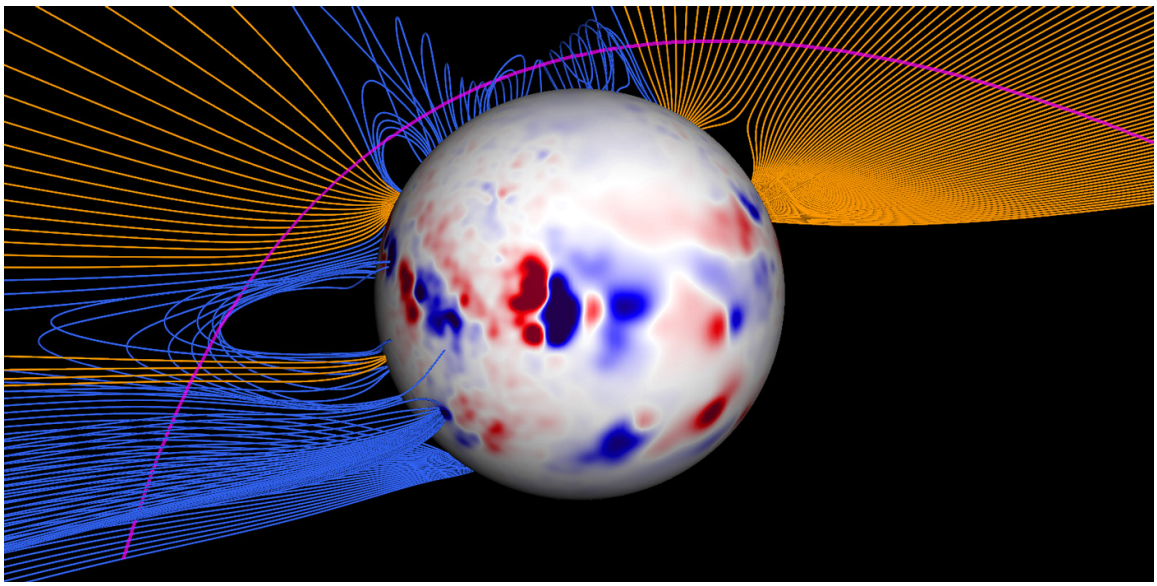

Figure S2: Visualization of the global magnetic field through which the comet passed. So that the entire trajectory can be seen, the viewing perspective is normal to the orbital plane. Field lines are drawn at points corresponding to 1 min intervals along the trajectory. Blue coloring indicates 'closed' field lines, and orange indicates 'open' field lines (one side passes through the $r = 20$ R_S boundary of the simulation).

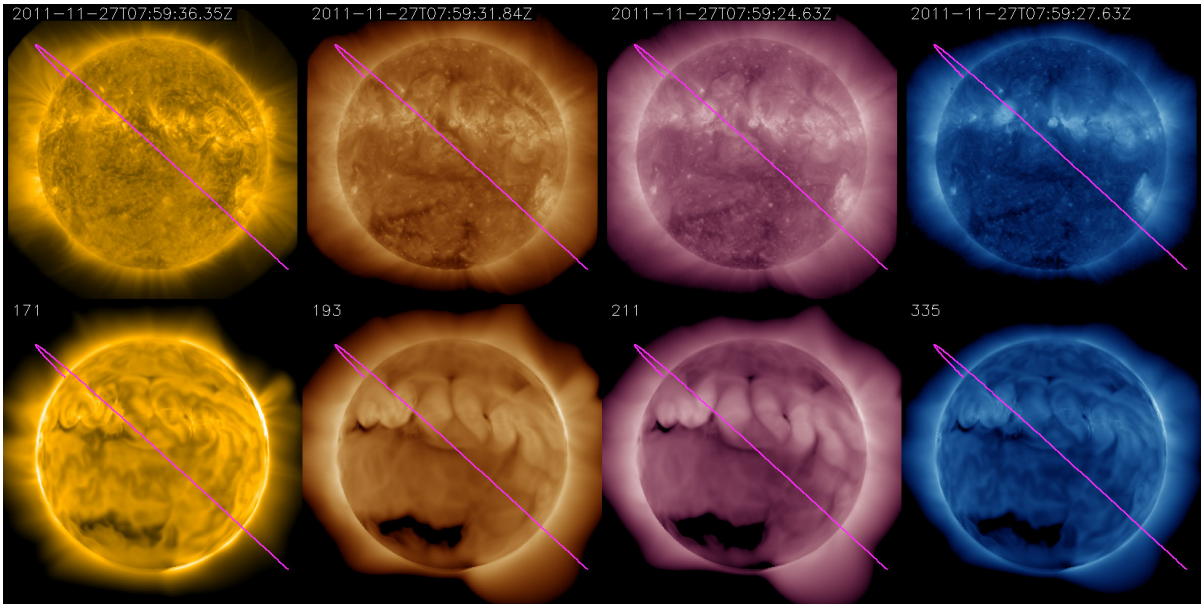

Figure S3: Comparison of AIA observations on 2011-11-27 nearest to 08:00 UT (Top) to synthetic observables from the thermodynamic solution (Bottom) for the AIA 171, 193, 211, and 335Å channels. These observations show the portion of the corona traversed by the comet during perihelion as it was observed on disk by AIA before rotating behind the sun.

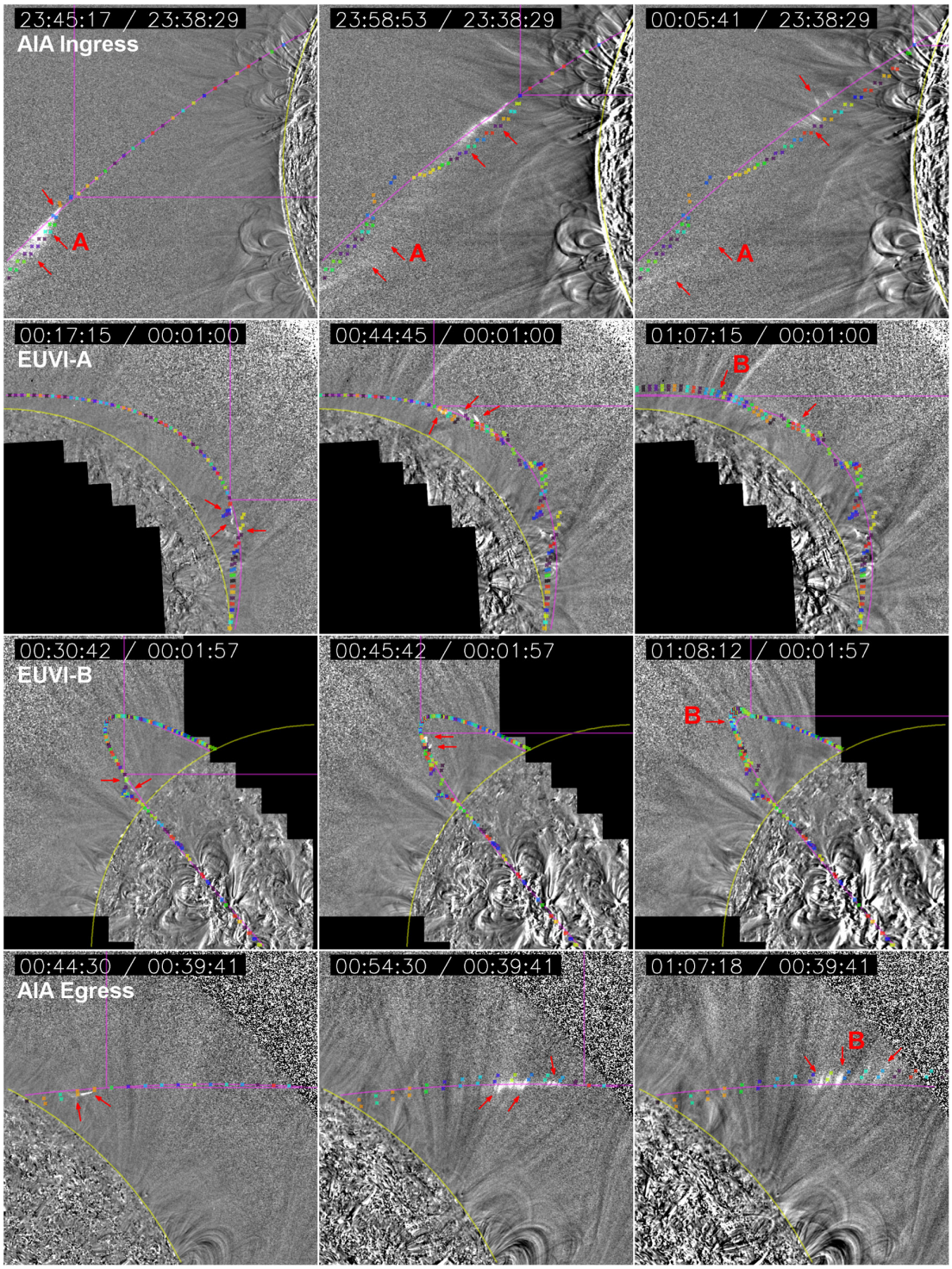

Figure S4: Visualization of the tail model applied to the global field of the thermodynamic MHD model for all four views. Time runs from left to right and views from top to bottom. As described in the text, the colored dots represent the predicted tail motion once the comet has passed. The time-dependent portion and final resting place of each dot depends on the comet velocity and orientation with respect to $\vec{B}$ according to Eq. (S8). The arrows mark locations where the comet tail is most visible, and highlight comparisons to the model prediction (dots). Region A (top row) depicts the non-radial motion of the tail in the southwest direction seen during the AIA Ingress. Region B (bottom three right panels) marks the tail as seen by three views at nearly the same state and location accounting for light travel time. This highlights the agreement between the predicted motion and observed tail location. Dot colors are consistent between frames.

References and Notes

1. *Solar Probe Plus: Report of the Science and Technology Definition Team*, NASA/TM-2008-214161 (2008).

2. B. G. Marsden, Sungrazing comets. *Annu. Rev. Astron. Astrophys.* **43**, 75 (2005). doi:10.1146/annurev.astro.43.072103.150554

3. Z. Sekanina, P. W. Chodas, Comet C/2011 W3 (Lovejoy): Orbit determination, outbursts, disintegration of nucleus, dust-tail morphology, and relationship to new cluster of bright sungrazers. *Astrophys. J.* **757**, 127 (2012). doi:10.1088/0004-637X/757/2/127

4. C. J. Schrijver *et al*., Destruction of Sun-grazing comet C/2011 N3 (SOHO) within the low solar corona. *Science* **335**, 324 (2012). doi:10.1126/science.1211688 Medline

5. M. J. Aschwanden *et al*., First three-dimensional reconstructions of coronal loops with the STEREO A + B spacecraft. IV. Magnetic modeling with twisted force-free fields. *Astrophys. J.* **756**, 124 (2012). doi:10.1088/0004-637X/756/2/124

6. R. A. Frazin, A. M. Vásquez, F. Kamalabadi, Quantitative, three-dimensional analysis of the global corona with multi-spacecraft differential emission measure tomography. *Astrophys. J.* **701**, 547 (2009). doi:10.1088/0004-637X/701/1/547

7. P. Bryans, W. D. Pesnell, The extreme-ultraviolet emission from sun-grazing comets. *Astrophys. J.* **760**, 18 (2012). doi:10.1088/0004-637X/760/1/18

8. See supplementary text S1 for details on the relevant time scales.

9. See supplementary materials and methods.

10. See supplementary text S2 and movies S5 to S8.

11. K. H. Schatten, J. M. Wilcox, N. F. Ness, A model of interplanetary and coronal magnetic fields. *Sol. Phys.* **6**, 442 (1969). doi:10.1007/BF00146478

12. P. Riley *et al*., A comparison between global solar magnetohydrodynamic and potential field source surface model results. *Astrophys. J.* **653**, 1510 (2006). doi:10.1086/508565

13. $\tau_{OV,OVI}$ is calculated using the sum of the inverse of the electron impact ionization rates for $O^{4+} \rightarrow O^{5+}$ and $O^{5+} \rightarrow O^{6+}$ at $n_e = 1 \times 10^8$ cm^{-3} obtained from table 2 of (*7*).

14. Y.-D. Jia, M. R. Combi, K. C. Hansen, T. I. Gombosi, A global model of cometary tail disconnection events triggered by solar wind magnetic variations. *J. Geophys. Res.* **112**, A05223 (2007). doi:10.1029/2006JA012175

15. Z. Sekanina, P. W. Chodas, Fragmentation hierarchy of bright sungrazing comets and the birth and orbital evolution of the Kreutz system. II. The case for cascading fragmentation. *Astrophys. J.* **663**, 657 (2007). doi:10.1086/517490

16. O. Burhonov *et al*., *Minor Planet Electronic Circulars* p. 63 (2012).

17. J. R. Lemen *et al*., The Atmospheric Imaging Assembly (AIA) on the Solar Dynamics Observatory (SDO). *Sol. Phys.* **275**, 17 (2012). doi:10.1007/s11207-011-9776-8

18. P. I. McCauley, S. H. Saar, J. C. Raymond, Y.-K. Ko, P. Saint-Hilaire, *Astrophys. J.* **768**, 161 (2013).

19. M. L. Kaiser *et al*., The STEREO mission: An introduction. *Space Sci. Rev.* **136**, 5 (2008). doi:10.1007/s11214-007-9277-0

20. J. Wuelser *et al*., in *Society of Photo-Optical Instrumentation Engineers Conference Series*, S. Fineschi, M. A. Gummin, Eds. (SPIE, Bellingham, WA, 2004), vol. 5171, pp. 111–122.

21. P. Saint-Hilaire *et al*., *American Astronomical Society Meeting Abstracts* (2012), vol. 220, p. 521.07; http://adsabs.harvard.edu/abs/2012AAS...22052107S.

22. Z. Mikić, J. A. Linker, Disruption of coronal magnetic field arcades. *Astrophys. J.* **430**, 898 (1994). doi:10.1086/174460

23. J. A. Linker, Z. Mikić, in *Coronal Mass Ejections*, N. Crooker, J. Joselyn, J. Feynmann, Eds. (American Geophysical Union, Washington, DC, 1997), pp. 269–277.

24. R. Lionello, Z. Mikić, J. A. Linker, Stability of algorithms for waves with large flows. *J. Comput. Phys.* **152**, 346 (1999). doi:10.1006/jcph.1999.6250

25. Z. Mikić, J. A. Linker, D. D. Schnack, R. Lionello, A. Tarditi, Magnetohydrodynamic modeling of the global solar corona. *Phys. Plasmas* **6**, 2217 (1999). doi:10.1063/1.873474

26. J. A. Linker, R. Lionello, Z. Mikić, T. Amari, Magnetohydrodynamic modeling of prominence formation within a helmet streamer. *J. Geophys. Res.* **106**, 25165 (2001). doi:10.1029/2000JA004020

27. R. Lionello, J. A. Linker, Z. Mikić, Including the transition region in models of the large-scale solar corona. *Astrophys. J.* **546**, 542 (2001). doi:10.1086/318254

28. P. H. Scherrer *et al*., The Helioseismic and Magnetic Imager (HMI) investigation for the Solar Dynamics Observatory (SDO). *Sol. Phys.* **275**, 207 (2012). doi:10.1007/s11207-011-9834-2

29. C. J. Schrijver, M. L. De Rosa, *Sol. Phys.* **212**, 165 (2003). doi:10.1023/A:1022908504100

30. P. H. Scherrer *et al*., The Solar Oscillations Investigation–Michelson Doppler Imager. *Sol. Phys.* **162**, 129 (1995). doi:10.1007/BF00733429

31. Y. Liu *et al*., Comparison of line-of-sight magnetograms taken by the Solar Dynamics Observatory/Helioseismic and Magnetic Imager and Solar and Heliospheric Observatory/Michelson Doppler Imager. *Sol. Phys.* **279**, 295 (2012). doi:10.1007/s11207-012-9976-x

32. R. Lionello, J. A. Linker, Z. Mikić, Multispectral emission of the Sun during the first whole Sun month: Magnetohydrodynamic simulations. *Astrophys. J.* **690**, 902 (2009). doi:10.1088/0004-637X/690/1/902

33. C. Downs *et al*., Toward a realistic thermodynamic magnetohydrodynamic model of the global solar corona. *Astrophys. J.* **712**, 1219 (2010). doi:10.1088/0004-637X/712/2/1219

34. C. Downs *et al*., Studying extreme ultraviolet wave transients with a digital laboratory: Direct comparison of extreme ultraviolet wave observations to global magnetohydrodynamic simulations. *Astrophys. J.* **728**, 2 (2011). doi:10.1088/0004-637X/728/1/2

35. C. Downs, I. I. Roussev, B. van der Holst, N. Lugaz, I. V. Sokolov, Understanding SDO/AIA observations of the 2010 June 13 EUV wave event: Direct insight from a global thermodynamic MHD simulation. *Astrophys. J.* **750**, 134 (2012). doi:10.1088/0004-637X/750/2/134

36. E. Landi, P. R. Young, K. P. Dere, G. Del Zanna, H. E. Mason, CHIANTI—an atomic database for emission lines. XIII. Soft x-ray improvements and other changes. *Astrophys. J.* **763**, 86 (2013). doi:10.1088/0004-637X/763/2/86

37. Guide to SDO Data Analysis, www.lmsal.com/sdodocs/doc/dcur/SDOD0060.zip/.

38. G. E. Brueckner *et al*., The Large Angle Spectroscopic Coronagraph (LASCO). *Sol. Phys.* **162**, 357 (1995). doi:10.1007/BF00733434

39. SOHO LASCO CME Catalog, http://cdaw.gsfc.nasa.gov/CME_list/.

40. P. M. Bellan, *Fundamentals of Plasma Physics* (Cambridge Univ. Press, Cambridge, 2006).

41. A. H. Delsemme, The chemistry of comets. *Philos. Trans. R. Soc. London Ser. A* **325**, 509 (1988). doi:10.1098/rsta.1988.0064

42. E. Landi *et al*., CHIANTI—an atomic database for emission lines. VII. New data for x-rays and other improvements. *Astrophys. J. Suppl. Ser.* **162**, 261 (2006). doi:10.1086/498148

43. These two terms are not strictly correct here until the ions have thermalized with the medium; however, these are small effects before deceleration has completed.

44. L. L. Williams, G. P. Zank, Effect of magnetic field geometry on the wave signature of the pickup of interstellar neutrals. *J. Geophys. Res.* **99**, 19229 (1994). doi:10.1029/94JA01657

Supplementary Movie Legends

Movie S1: Base ratio processed AIA 171Å observations of Comet Lovejoy's ingress into the corona before perihelion. The magenta arc indicates the orbital trajectory and the intersection of the horizontal and vertical lines indicates the predicted position of the comet nucleus at the observation time.

Movie S2: Base ratio processed EUVI-A 171Å observations of Comet Lovejoy's perihelion passage. The magenta arc indicates the orbital trajectory and the intersection of the horizontal and vertical lines indicates the predicted position of the comet nucleus at the observation time.

Movie S3: Base ratio processed EUVI-B 171Å observations of Comet Lovejoy's perihelion passage. The magenta arc indicates the orbital trajectory and the intersection of the horizontal and vertical lines indicates the predicted position of the comet nucleus at the observation time.

Movie S4: Base ratio processed AIA 171Å observations of Comet Lovejoy's egress from the corona after perihelion. The magenta arc indicates the orbital trajectory and the intersection of the horizontal and vertical lines indicates the predicted position of the comet nucleus at the observation time.

Movie S5: Visualization of the dynamical tail model applied to the MHD solution overlaid over AIA observations of the ingress. As described in Section S2 and Fig. S4, the colored dots follow the predicted tail motion once the comet has passed.

Movie S6: Visualization of the dynamical tail model applied to the MHD solution overlaid over EUVI-A observations of perihelion. As described in Section S2 and Fig. S4, the colored dots follow the predicted tail motion once the comet has passed.

Movie S7: Visualization of the dynamical tail model applied to the MHD solution overlaid over EUVI-B observations of perihelion. As described in Section S2 and Fig. S4, the colored dots follow the predicted tail motion once the comet has passed.

Movie S8: Visualization of the dynamical tail model applied to the MHD solution overlaid over AIA observations of the egress. As described in Section S2 and Fig. S4, the colored dots follow the predicted tail motion once the comet has passed.